

## Age relationship of basaltic and andesitic surface compositions on Mars: Analysis of high-resolution TES observations of the northern hemisphere

Deanne Rogers and Philip R. Christensen

Department of Geological Sciences, Arizona State University, Tempe, Arizona, USA

Received 11 April 2002; revised 31 October 2002; accepted 5 November 2002; published 26 April 2003.

[1] Previous Mars Global Surveyor Thermal Emission Spectrometer (TES) results have identified two principal surface compositions on Mars; basaltic surfaces are found primarily in the southern highlands, while andesitic surfaces are found in the northern lowlands and in smaller concentrations distributed throughout the southern highlands. In 1 pixel-per-degree composition maps, the exact boundary between the basaltic and andesitic compositions is obscured by large amounts of equatorial surface dust. In this work, high-resolution TES surface spectral data are used to identify and characterize isolated regions of basalt within the equatorial dust regions and northern lowlands (generally between 20°S–60°N, 0–360°W) in an effort to better understand the nature of the boundary between the two compositions. The purpose of refining this boundary is to more accurately determine the relationship of the compositional dichotomy with global surface morphology and derived crustal thickness. Results show that the basaltic surface composition is closely associated with the ancient cratered terrain morphology but is not well correlated with crustal thickness. The northern extent of the TES basalt composition is also established. With four exceptions, there are no significant concentrations (>~30% surface cover) of basalt greater than ~400 km<sup>2</sup> in area within the northern plains. Three are located within or adjacent to knobby terrain, which has been suggested to be erosional remnants of the cratered highlands. The fourth exception is in Milankovic crater and may represent a local basalt flow or basaltic material excavated during crater formation. Results from this work suggest that there is a stratigraphic relationship between the basaltic and andesitic surface compositions, with younger andesitic materials overlying older basaltic materials throughout the equatorial and northern plains regions. *INDEX TERMS*: 5464 Planetary Sciences: Remote sensing; 5480 Planetary Sciences: Volcanism (8450); 5470 Planetary Sciences: Surface materials and properties; 8450 Volcanology: Planetary volcanism (5480); *KEYWORDS*: Mars volcanics, Mars surface compositions, Mars basalt, Thermal Emissions Spectrometer, basalt outliers

**Citation:** Rogers, D., and P. R. Christensen, Age relationship of basaltic and andesitic surface compositions on Mars: Analysis of high-resolution TES observations of the northern hemisphere, *J. Geophys. Res.*, 108(E4), 5030, doi:10.1029/2002JE001913, 2003.

### 1. Introduction

[2] Photogeologic, gravimetric and spectral observations from the Mariner, Viking, and Mars Global Surveyor (MGS) missions have shown that Mars exhibits global dichotomies in the geomorphology [e.g., *Masursky*, 1973], crustal thickness [*Zuber et al.*, 2000], and composition [*Bandfield et al.*, 2000a]. Images from Mariner 9 [*Masursky*, 1973] and Viking showed that Mars is heavily cratered in the southern highlands and has smooth plains in the northern lowlands. The smooth plains were most likely formed by the resurfacing of a heavily cratered, older terrain by volcanic and/or aeolian processes [*Tanaka et al.*, 1992; *Zuber et al.*, 2000; *Head et al.*, 2002]. The MGS Mars Orbiter Laser Altimeter (MOLA) observations have

revealed that there are two major zones of crustal thickness, with the northern lowlands having a uniformly thin crust, while the southern highlands have a thick crust [*Zuber et al.*, 2000]. Unlike the morphology, however, crustal thickness gradually thins towards the north, rather than having a sharp boundary [*Zuber et al.*, 2000]. The crustal thickness boundary and the morphologic boundary are not correlated everywhere. The largest region of divergence between the two boundaries is Arabia Terra, which has the crustal thickness of the northern lowlands, but the heavily cratered geomorphology of the southern highlands. For this reason, *Zuber et al.* [2000] suggested that Arabia Terra may be a region of exposed northern lowland basement. Lastly, spectral observations from the MGS Thermal Emission Spectrometer (TES) have shown that a compositional dichotomy exists as well; the majority of low-albedo surfaces in the southern highlands are composed of basalt to low-Si basaltic andesite, while low-albedo surfaces in the

northern lowlands, as well as several areas in the highlands, are composed of high-Si basaltic andesite to andesite [Bandfield *et al.*, 2000a].

[3] In light of the above MGS observations, it is suggested here that references to the “dichotomy” on Mars should be supported by the appropriate adjective (e.g., “morphologic dichotomy,” “topographic dichotomy,” “compositional dichotomy”). In addition, the terms “southern highlands” (referring to topography) and “cratered terrain” (referring to morphology) are not completely synonymous. In areas such as Arabia Terra, the topography of the cratered terrain gradually decreases towards the north, and is  $\sim 3$  km lower than the rest of the “highlands.” To avoid confusion when referring to morphology, the global morphologic provinces of heavily cratered terrain and lowland plains are hereafter referred to in this work as the “cratered terrain” and “northern smooth plains,” instead of “southern highlands” and “northern lowlands.”

[4] The rough correlation of basaltic and andesitic surface compositions with the older cratered terrain and the younger northern plains, respectively [Bandfield *et al.*, 2000a], raises the question of whether there has been an evolution of magma composition with time. In an effort to answer this question, this work uses high-resolution compositional information derived from TES observations to determine the association between lithology and the morphologic dichotomy on Mars.

[5] To associate lithology with surface geology, it is imperative that the areal extent of the basaltic and andesitic surface compositions is known. However, in the low-resolution compositional distribution maps of Bandfield *et al.* [2000a], the boundary between the two spectral units is difficult to resolve owing to large regions of equatorial surface dust that obscure the composition of the underlying bedrock. In this work, high-resolution (32 pixel-per-degree) TES data are used to identify small, isolated regions of particulate basalt within the equatorial dust regions and the northern lowlands in an effort to better define the location of this boundary. If the basaltic materials are derived from the nearby bedrock, then the isolated regions can be considered “windows” for detecting the bedrock composition beneath the thick dust deposits. Thus in this study, constraints on the source of the basalt in each isolated area are especially important. It is necessary to assess whether the materials are “local” (defined here as the original bedrock source being within a radius of a few hundred kilometers) or “regional” if they have been transported in from further away (several hundred to greater than a thousand kilometers) via saltation.

## 2. Background

### 2.1. TES Observations

#### 2.1.1. Linear Deconvolution of Thermal Emission Spectra and Mineral Abundance Determination

[6] Thermal emission spectroscopy has been shown to be a quantitative analytical technique for remotely determining the modal mineralogy of geologic surfaces in the laboratory, in the field, and from airborne and spaceborne platforms. A measured emission spectrum from a geologic surface can be modeled as the sum of the spectra of each mineral component weighted by the areal fraction of that component [e.g., Gillespie, 1992; Thomson and Salisbury, 1993; Ramsey and

Christensen, 1998; Feely and Christensen, 1999; Hamilton and Christensen, 2000]. Therefore it is possible to compute the mineral areal abundances of remote surfaces using linear deconvolution techniques [Gillespie, 1992; Ramsey and Christensen, 1998; Ramsey *et al.*, 1999]. Taking into consideration the TES spatial resolution, spectral range, signal-to-noise ratio, and atmospheric removal uncertainties, the mineral abundance detection limit for TES emissivity spectra has been estimated to be  $\sim 10$ – $15\%$  [e.g., Christensen *et al.*, 2000a]. Based on the linear deconvolution technique, TES data have been used to determine the dominant rock types found on the Martian surface [Bandfield *et al.*, 2000a; Christensen *et al.*, 2000a; Christensen *et al.*, 2000b; Hoefen *et al.*, 2000; Hamilton *et al.*, 2001b].

#### 2.1.2. Effective Emissivity Determination and Surface-Atmosphere Separation

[7] The thermal radiance spectrum collected from each TES observation is converted to an effective emissivity spectrum, which is defined as the ratio of the radiance spectrum divided by a Planck function that corresponds to the maximum brightness temperature in the measured radiance spectrum. Prior to determining the maximum brightness temperature, a boxcar filter with a  $50\text{ cm}^{-1}$  bandwidth is applied to the radiance spectrum. This reduces the effect of noise in the temperature determination. The measured radiance is a combination of radiance from both the atmosphere and surface throughout the entire TES spectral range. Two independent surface-atmosphere separation techniques have been developed by Bandfield *et al.* [2000b] and Smith *et al.* [2000] specifically for the analysis of TES data in order to produce surface-only emissivity spectra. Both techniques are effective for accurately obtaining surface emissivity over varying atmospheric temperatures and dust and water ice opacities [Bandfield *et al.*, 2000b; Smith *et al.*, 2000]. The deconvolution algorithm is the surface-atmosphere separation technique utilized in the work presented here because it simultaneously returns surface endmember abundances and can be used on a “spectrum-by-spectrum” basis [Bandfield *et al.*, 2000b; Smith *et al.*, 2000]. The spectral regions used for surface analysis are reduced to  $\sim 1300$ – $825\text{ cm}^{-1}$  and  $\sim 525$ – $230\text{ cm}^{-1}$  due to exclusion of the atmospheric  $\text{CO}_2$  fundamental absorption at  $\sim 667\text{ cm}^{-1}$  and water vapor/lower signal-to-noise regions at wave numbers  $>\sim 1300\text{ cm}^{-1}$  and  $<\sim 225\text{ cm}^{-1}$  [e.g., Smith *et al.*, 2000; Bandfield, 2002]. For a complete review of TES instrument and data characteristics, see Christensen *et al.* [1992] and Christensen *et al.* [2001a].

#### 2.1.3. Identification and Mapping of Principal (Basaltic and Andesitic) Martian Surface Compositions

[8] Bandfield *et al.* [2000a] inspected surface emissivity spectra from 25 major low-albedo regions on Mars (TES albedo is measured using the VIS/NIR broadband radiometer, which is sensitive to wavelengths between  $0.3$  and  $2.9\text{ }\mu\text{m}$  [e.g., Christensen *et al.*, 2001a]). Upon examination of the representative surface spectra from each region, two different spectral shapes were apparent (Figure 1) [Bandfield *et al.*, 2000a]. One is common to Syrtis Major (Type I), while the other (Type II) is common to Acidalia Planitia. The surface spectral shapes were then deconvolved using an endmember subset from the ASU library of mineral spectra [Christensen *et al.*, 2000c], which consisted of  $\sim 60$  rock-forming and alteration minerals, with particle sizes ranging

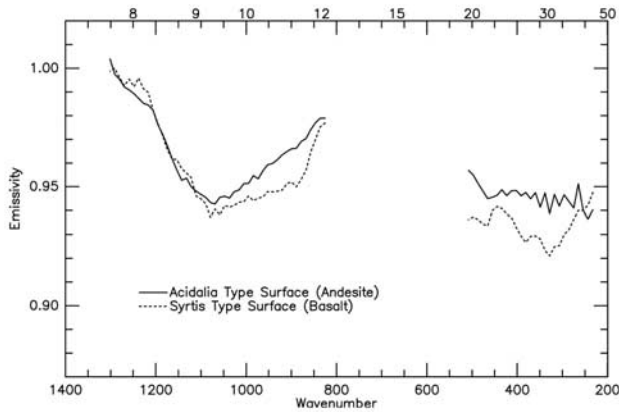


**Figure 1.** The two surface unit spectra of *Bandfield et al.* [2000a].

from 750 to 1000  $\mu\text{m}$  [*Bandfield et al.*, 2000a]. The relative mineral areal abundances in the Syrtis Major-type spectra are consistent with a basaltic surface (50% feldspar, 25% clinopyroxene, 15% sheet silicates); while the abundances in the Acidalia-type spectra (35% feldspar, 25% high-silica glass, 15% sheet silicates, 10% pyroxene) are consistent with a basaltic andesite/andesitic surface ( $\sim 57$  wt. % silica) [*Bandfield et al.*, 2000a]. The Syrtis Major type surface composition is hereafter also referred to as “basaltic surface” or “basalt,” and the Acidalia Planitia type surface composition is referred to as “andesitic surface” or “andesite.” Spectra of terrestrial particulate samples of basaltic andesite and flood basalt also proved to match well with the martian surface spectra [*Bandfield et al.*, 2000a; *Christensen et al.*, 2000a].

[9] Using linear deconvolution methods, *Bandfield et al.* [2000a] determined the global distribution of basalt and andesite at a spatial resolution of one pixel per degree (ppd) (Figure 2). From these global distribution maps (Figure 2), *Bandfield et al.* [2000a] concluded that the basaltic composition is mostly restricted to the southern cratered terrain, while the andesitic composition has the highest concentrations in the northern smooth plains, with lesser concentrations also distributed in the southern cratered terrain. At low spatial resolution, the large equatorial dust regions (mostly represented by either black or blue in Figure 2) make it difficult to determine exactly where the compositional boundary is and therefore to establish a precise association between this boundary and geomorphologic changes.

#### 2.1.4. Interpretation of the Surface Type 2 Spectrum

[10] The determination that large areas of Mars are composed of basalt came as no surprise; previous remote-sensing and SNC meteorite studies have shown that a basaltic lithology would be the expected composition of the majority of martian low-albedo surfaces [e.g. *Singer and McSween*, 1993; *Bell et al.*, 1997]. However, the considerable abundance of andesite revealed by TES data has been debated because on Earth, andesite is typically associated with subduction zones (although rocks of andesitic composition can also be produced through anorogenic processes) [e.g., *Carmichael*, 1964; *Gill*, 1981, p. 294]. There is no strong evidence for plate tectonics or subduction-related volcanism on Mars [e.g., *Carr*, 1973]. Thus other explanations for the

Type 2 surface spectrum have been put forth [e.g., *Minitti et al.*, 2002; *Wyatt and McSween*, 2002]. *Wyatt and McSween* [2002] demonstrate that the Type 2 surface spectrum can be well-modeled using potassium feldspar (14%), plagioclase

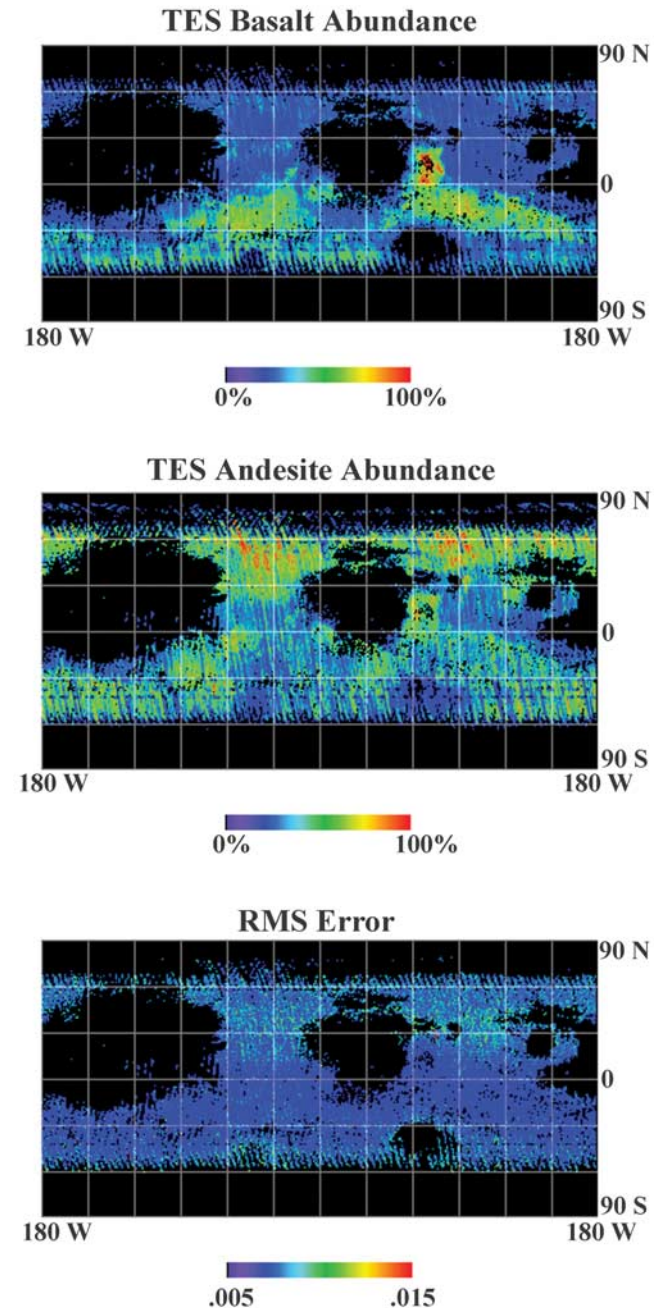


**Figure 2.** Global distributions of basalt and andesite concentrations (1ppd). Only surfaces with thermal inertia values  $>190 \text{ J/m}^2\text{Ks}^{1/2}$  are shown, which corresponds to an effective particle size of  $>\sim 100 \mu\text{m}$ , assuming a homogeneous unconsolidated surface [*Kieffer et al.*, 1977; *Presley and Christensen*, 1997]. This effective particle size was chosen because emission spectra of surfaces below the grain size range of  $\sim 63\text{--}125 \mu\text{m}$  are not well modeled with linear deconvolution techniques, when using spectral endmembers of mineral grains between 750 and 1000  $\mu\text{m}$  [*Ramsey and Christensen*, 1998]. RMS error is also shown. The distributions are from *Bandfield et al.* [2000a].

(25%), pyroxene (16%), and clay minerals (31%). This model result only occurs when high-silica glass is excluded from the endmember set; when high-silica glass is allowed, model fits are improved [Hamilton *et al.*, 2002]. Wyatt and McSween [2002] compare the distribution of Type 2 surfaces in the northern lowlands with an area previously suggested to be the site of an ancient ocean [e.g., Parker *et al.*, 1993]. They conclude with an alternative interpretation for the Type 2 spectrum: that it instead represents a basaltic surface weathered in a submarine environment. The spectral similarities between high-silica glass and sheet-silicate weathering products are the cause for the two very different interpretations [Bandfield, 2002]. Therefore because of the difficulty in differentiating glass from clays in emissivity spectra, other lines of evidence must be used to distinguish glass-rich andesitic surfaces from heavily weathered basaltic surfaces on Mars.

[11] First, high concentrations of the Type 2 spectrum are found south of the proposed shorelines, including parts of Syrtis Major and southern highlands areas south of  $\sim 40^\circ\text{S}$  [Bandfield *et al.*, 2000a; Bandfield, 2002] (see also Figure 2). These include areas where ancient oceans and other water-related processes have not been suggested to exist and therefore a second interpretation, in addition to basalt altered in a submarine environment, would still be required to explain the Type 2 surface concentrations in both the lowland plains and the southern highland areas [Hamilton *et al.*, 2002]. Second, Acidalia Planitia and other regions that exhibit the Type 2 spectrum consist of sand-sized particles [Bandfield *et al.*, 2000a; Mellon *et al.*, 2000]. This includes the north polar sand dunes, which have strong Type 2 spectral signatures [Bandfield, 2002; Bandfield *et al.*, 2002]. It is unlikely that significant amounts of sheet-silicate weathering products would exist on active, saltating sand grains [Bandfield, 2002; Hamilton *et al.*, 2002]. Third, the Mars Pathfinder APXS revealed elevated amounts of silica in the landing site rocks. Although the initially-reported amounts of silica decreased by  $\sim 10\%$  after recent recalibration, the corrected amount of silica ( $\sim 57\%$ ) [Foley *et al.*, 2000; Brückner *et al.*, 2001] is still on the border between terrestrial basaltic andesite and andesite fields and is actually the exact abundance of silica reported by Bandfield *et al.* [2000a] and Hamilton *et al.* [2001a] for the Type 2 surface. Finally, near-infrared reflectance observations are highly sensitive to clay mineralogies and do not show evidence for significant amounts of clays in the low-albedo regions of Mars [e.g., Soderblom, 1992]. Based on the above evidence, presently the simplest explanation for the spectral shape common to Acidalia Planitia (Type 2) is that it is glass-rich andesite [Hamilton *et al.*, 2002]; however, alternative explanations for silica-enrichment are certainly possible [e.g., Morris *et al.*, 2000]. In this work the Type 2 surface is interpreted as a primary volcanic andesitic composition, and results are used to understand the relationship between the distribution of basaltic and andesitic compositions.

## 2.2. Aeolian Transport of Sand

### 2.2.1. Previous Work on Martian Sand Transport

[12] The subject of aeolian sand transport on Mars has been studied extensively by previous authors [e.g., Iversen *et al.*, 1976; Sagan *et al.*, 1977; Krinsley *et al.*, 1979;

White, 1979; Greeley *et al.*, 1980; Greeley and Iversen, 1985; Edgett and Christensen, 1991; Anderson *et al.*, 1999], who use methods such as wind-tunnel experiments, numerical solutions, and photogeologic observations to predict the behavior of windblown sand particles on the martian surface.

[13] Because previous experiments [e.g., White, 1979; Greeley *et al.*, 1980; Edgett and Christensen, 1991] provide the threshold friction speeds and trajectory path lengths for varying Martian atmospheric pressures, temperatures, surface friction heights, and particle diameters, it is possible to calculate transport distances for various grain sizes on Mars. However, one other, less-constrained factor that must be accounted for is particle attrition or reduction in particle size per saltation impact.

[14] Degradation rates for saltating particles have been studied by Krinsley *et al.* [1979] and Krinsley and Greeley [1986]. To perform aeolian abrasion experiments, they use a Mars Erosion Device (MED), which simulates saltation by using a rotating “paddle-wheel” to propel sand up against a surface in the ceiling of the apparatus. They report decreases in grain size after the sand “saltated” for various periods of time and confirm that collisions on Mars are indeed more energetic than on Earth [Krinsley *et al.*, 1979; Krinsley and Greeley, 1986]. Greeley and Kraft [2001] use the MED to abrade quartz and basaltic sand between 500–600  $\mu\text{m}$  in diameter, at 1000RPM (equivalent to  $\sim 8$  m/s). By assuming that one paddle-wheel rotation equals one saltation impact, they are able to estimate the number of saltation impacts it takes to reduce the particle diameter by a certain amount.

### 2.2.2. Estimated Transport Distance for Basaltic Sand on Mars

[15] Knowing the previous estimates of particle degradation [Greeley and Kraft, 2001] and of path lengths, calculated as a function of particle diameter [White, 1979; Edgett and Christensen, 1991], it is possible to estimate the distance that sand can travel before it is degraded into a size not amenable to saltation transport ( $< \sim 115$   $\mu\text{m}$ ). Attrition data from Greeley and Kraft [2001] showed that basaltic sand grains with an initial average diameter of 550  $\mu\text{m}$  were degraded to 470  $\mu\text{m}$  after 360 minutes of abrasion at particle speeds of  $\sim 8$  m/s. This rate is equivalent to the diameter loss of 80  $\mu\text{m}$  per 360,000 saltation impacts or 1  $\mu\text{m}$  per  $\sim 4500$  saltation impacts. Edgett and Christensen [1991] derive a path length of  $\sim 30$  cm for 550  $\mu\text{m}$  grains initially at rest, using an atmospheric pressure of 5 mbar, temperature of 240 K, and a particle density of 2.65 g/cm<sup>3</sup>. Thus using this path length, 550  $\mu\text{m}$  sand should lose 1  $\mu\text{m}$  per  $\sim 1.35$  km of saltation. Note that this is a minimum erosion rate per distance traveled since it assumes the full transport distance in each impact. Table 1 shows the transport distances estimated in this manner for varying grain sizes. Increasing path lengths with decreasing particle size are taken into account. These transport distance estimates are calculated by using the diameter loss rate of 1  $\mu\text{m}$  per 4500 impacts, multiplying by the path length, and adding that distance to the distance already traveled. Note that the distances are calculated from a starting grain size of 550  $\mu\text{m}$  because this is the starting diameter used in the particle attrition experiments of Greeley and Kraft [2001].

[16] One assumption made in these estimates (Table 1) is that the particle diameter degrades linearly with each

**Table 1.** Estimates of Maximum Aeolian Transport Distances for Varying Grain Sizes<sup>a</sup>

D <sub>p</sub> , microns	Path Length 1 <sup>b</sup> , cm	Path Length 2 <sup>b</sup> , cm	Transport Distance <sup>c</sup> , km
550	30	30	0
500	32	37	7283
400	38	55	243–330
300	42	68	432–636
200	57	108	689–1122
115	90	175	1033–1791

<sup>a</sup>Maximum transport distances are calculated from a starting diameter of 550 microns (starting average particle diameter in the attrition experiments of *Greeley and Kraft* [2001]). A degradation rate of 1 micron per 4500 impacts is used.

<sup>b</sup>Path lengths are from *Edgett and Christensen* [1991]. Path length 1 is for particle ejection from a saltating grain, and path length 2 is for particle ejection from a bed of grains initially at rest.

<sup>c</sup>Cumulative transport distance from starting size of 550 microns.

impact. However, *Greeley and Kraft* [2001] show that the particles degrade faster initially, while the amount of degradation decreases after a number of impacts owing to the increased rounding of grains. Despite this assumption, these rough estimates of travel distance for each particle size should be thought of as conservative upper limits, because they do not account for the effect of topographic sand trapping (for example, trapping by craters). This effect has been shown to influence the distribution of sand on Mars and is likely to be important in limiting the distance that sand can travel [*Christensen*, 1983; *Thomas*, 1985; *Anderson et al.*, 1999].

[17] Supporting evidence for these transport estimates comes from previous MGS TES results. The existence of distinct, spatially separated surface units of basalt and andesite [*Bandfield et al.*, 2000a], crystalline hematite [*Christensen et al.*, 2000b; *Christensen et al.*, 2001b], and olivine [*Hoefen et al.*, 2000; *Hamilton et al.*, 2001b] on Mars

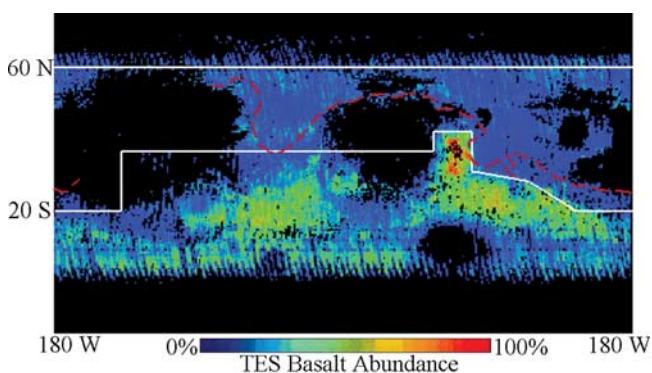


**Figure 3.** The area between the white lines is the study region (approximately between 20°S–60°N, 0–360°W) used for high-resolution mapping and identification of small isolated basalt regions, shown on the basalt concentration map of *Bandfield et al.* [2000a]. As in Figure 2, areas with low thermal inertia values are black. This area was chosen in order to include the large equatorial dust areas, as well as the morphologic and crustal dichotomy boundaries. The dark red line is an approximation of the morphologic dichotomy boundary.

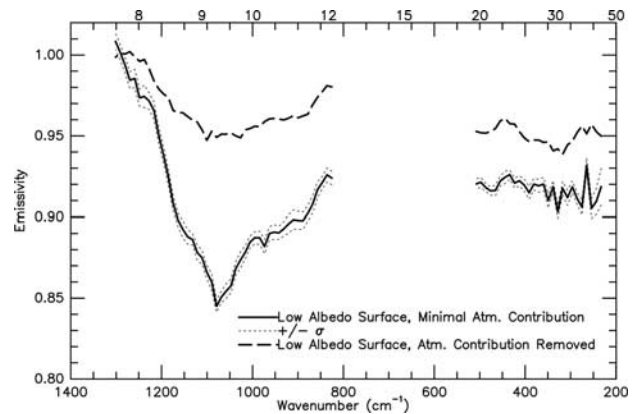


**Figure 4.** An effective emissivity spectrum (an average of 30 individual spectra) with low atmospheric dust and water ice loading compared with the resultant atmospherically corrected surface emissivity spectrum.

is a basic indicator that global mixing of sand-sized particles has not occurred. As mentioned earlier, the basaltic and andesitic surface compositions have the spectral contrast and thermal inertia consistent with sand-sized particles. If global-scale transport were taking place, it is likely that only one surface spectral shape, representing a mixture of the two original compositions, would be detected. (Surface spectra consistent with mixtures of basaltic and andesitic sediments have been detected on smaller spatial scales [*Bandfield et al.*, 2000a], however, suggesting that some degree of transport is occurring). The crystalline hematite regions of Sinus Meridiani, Aram Chaos, and Valles Marineris [*Christensen et al.*, 2000b; *Christensen et al.*, 2001b] can also be used to constrain transport distance of sand on Mars. The regions consist of basalt and hematite, with hematite abundances ranging from ~10–60%, depending on the actual particle size of the hematite. Thermal inertia values indicate that the average particle size of the surface materials in these regions ranges from 800–900  $\mu\text{m}$ . If it is assumed that (1) the hematite in each of these regions crystallized in their present locations, (2) the hematite is associated with the basaltic sand grains, and (3) the hematite is not acting as a cement, then the farthest that any basalt-hematite sand could have been transported is the maximum diameter of the largest region, Sinus Meridiani, which is approximately 550 km. This distance is likely an upper limit because the boundary of the hematite unit is distinct (hematite index values decrease from high to background level over a distance of <10 km), suggesting little transport of hematite away from its source region [*Christensen et al.*, 2001b].

### 3. Approach

[18] The objectives of this work are to determine the association of composition with morphology and to more sharply define the northern extent of the basaltic surface composition. This study specifically addresses the global morphologic provinces of ancient, heavily cratered terrain and less-cratered, northern smooth plains. These terrains represent large-scale variations in surface age, based on differences in crater densities [e.g., *Strom et al.*, 1992]. A correlation of composition with geomorphology (and thus

**Table 2.** Mineral Endmembers Used in Deconvolution of Emissivity Spectra From Each Basalt Region<sup>a</sup>

Mineral Name <sup>b</sup>	Mineral ID
Quartz	BUR-4120
Microcline	BUR-3460
Albite	WAR-0244
Oligoclase	BUR-060D
Andesine	BUR-240
Labradorite	WAR-4524
Bytownite	WAR-1384
Anorthite	BUR-340
Enstatite	HS-9.4B
Bronzite	NMNH-93527
Diopside	WAR-6474
Augite	NMNH-9780
Augite	NMNH-122302
Hedenbergite, Manganoan	DSM-HED01
Forsterite	AZ-01
Fayalite	WAR-RGFAY01
Hematite	BUR-2600
Anhydrite	ML-S9
Gypsum	ML-S6
Calcite	C27
Siderite	C62
Actinolite	HS-166.4B
Biotite	BUR-840
Muscovite	WAR-5474
Chlorite	WAR-1924
Serpentine	HS-8.4B
Serpentine	BUR-1690
Nontronite	WAR-5108g granular
Kaolinite	Kga-1b granular
Illite	Imt-2g granular
SiK glass	MW-SiK-GLASS
Apatite	ML-P1

<sup>a</sup>For chemical formulas, please see <http://tes.la.asu.edu/speclib/index.html>.

<sup>b</sup>Mineral groups from top to bottom: quartz, feldspar, pyroxene, olivine, hematite, sulfate, carbonate, amphibole, sheet-silicates/glass, phosphate.

surface age) could have implications towards a change in magma composition with time. As mentioned above, it is difficult to define the exact boundary between the basalt and andesite on the low-resolution one pixel-per-degree (1 ppd, equal to  $\sim 3600 \text{ km}^2/\text{pixel}$  at the equator) maps of *Bandfield et al.* [2000a] owing to large amounts of surface dust that obscure the boundary region (Figure 2). However, by mapping the surface at a higher resolution (32 ppd,  $\sim 3.5 \text{ km}^2/\text{pixel}$  at the equator), isolated regions of low-albedo materials can be located within the surrounding dusty areas and their composition can be determined. Thus when the basaltic surface composition is mapped at the highest possible resolution, small regions of basalt that correspond to the isolated low-albedo materials can be distinguished. The basaltic surface type was chosen for the focus of this study (rather than andesite) because it has a more well defined distribution in the abundance maps of *Bandfield et al.* [2000a] (Figure 2), relative to the andesitic surface distribution. It is easier to define the northern extent of the basaltic surface composition, rather than the southern extent of the andesitic surface type.

[19] The basaltic materials in these regions have been estimated to have transport distances that are small relative to the scale of geologic features observable with TES (Table 1); therefore the materials are likely to be derived

from bedrock within a few hundred kilometers of their present locations. This allows the isolated regions to be used to greatly narrow the compositional boundary zone because they are considered to be representative of nearby bedrock that is buried under dust.

### 3.1. Identification of Isolated Basalt Regions

[20] Using the atmospheric-correction and unit-mapping techniques of *Bandfield et al.* [2000a, 2000b] (above, section 2.1.3), concentrations of the basaltic surface composition were computed and mapped at a resolution of 32 ppd, generally between  $20^\circ\text{S}$ – $60^\circ\text{N}$ ,  $0$ – $360^\circ\text{W}$  (Figure 3). These coordinates were selected in order to find small areal distributions of basalt within the northern lowlands and large dusty regions and to focus on areas near the crustal and morphologic dichotomy boundaries. Only spectra that were collected from low emission angles ( $<30^\circ$ ), warm surfaces ( $>255 \text{ K}$ ), and low atmospheric dust and ice extinctions ( $<0.18$  and  $<0.10$ , respectively) were used. The resulting map was then examined in  $20^\circ \times 20^\circ$  areas, in order to find areally small, elevated concentrations of basalt. Basalt abundances shown in these concentration maps are not normalized for blackbody or atmospheric contribution [after *Bandfield et al.*, 2000a].

[21] When using these unit-mapping techniques, derived surface-type abundances can sometimes be affected by non-ideal conditions such as surface fines or the presence of higher atmospheric water ice and dust loadings. To confirm the basalt concentrations identified for each region in these maps, it is necessary to visually inspect the surface spectra for each region. For example, at longer wavelengths ( $\sim 20$ – $40 \mu\text{m}$ , or  $\sim 500$ – $250 \text{ cm}^{-1}$ ), the basaltic and andesitic spectral shapes exhibit distinctive features (see Figure 1). There are two concave downward spectral features (local emission maxima) at  $\sim 450 \text{ cm}^{-1}$  and  $\sim 360 \text{ cm}^{-1}$  that are recognizable in basaltic surface spectra, as well as a general V-shaped feature centered at  $\sim 325 \text{ cm}^{-1}$ . The long wavelength range is especially useful because dust opacity is low within this spectral region. Although each surface spectrum is examined in its entirety ( $\sim 1300$ – $825 \text{ cm}^{-1}$ ,  $\sim 525$ – $230 \text{ cm}^{-1}$ ), the existence of these spectral features at long wavelengths is the strongest indicator that a basaltic surface component is present.

[22] To inspect the surface spectra, TES effective emissivity spectra were first retrieved for each candidate region. The spectra used were from MGS Mapping Phase Orbits between  $L_s$  104–352 (TES orbit counts 1600–7000), and taken from warm surfaces ( $>255 \text{ K}$ ) and low emission angles ( $<30^\circ$ ). Effective emissivity spectra that are from low-albedo surfaces and that have the least atmospheric contribution were averaged together for each region. Note that averaging does not decrease the spatial resolution because spectra are taken from repeat observations. Anywhere from 6 to 50 spectra were used in each average. The averaged spectra were deconvolved using the same surface-atmosphere separation techniques described in *Bandfield et al.* [2000a, 2000b]. The resultant surface spectra (Figure 4) for each region were then visually compared with the basalt and andesite endmembers to verify the surface composition of that region.

[23] Although the qualitative approach of visual inspection is important, it is also necessary to quantitatively assess

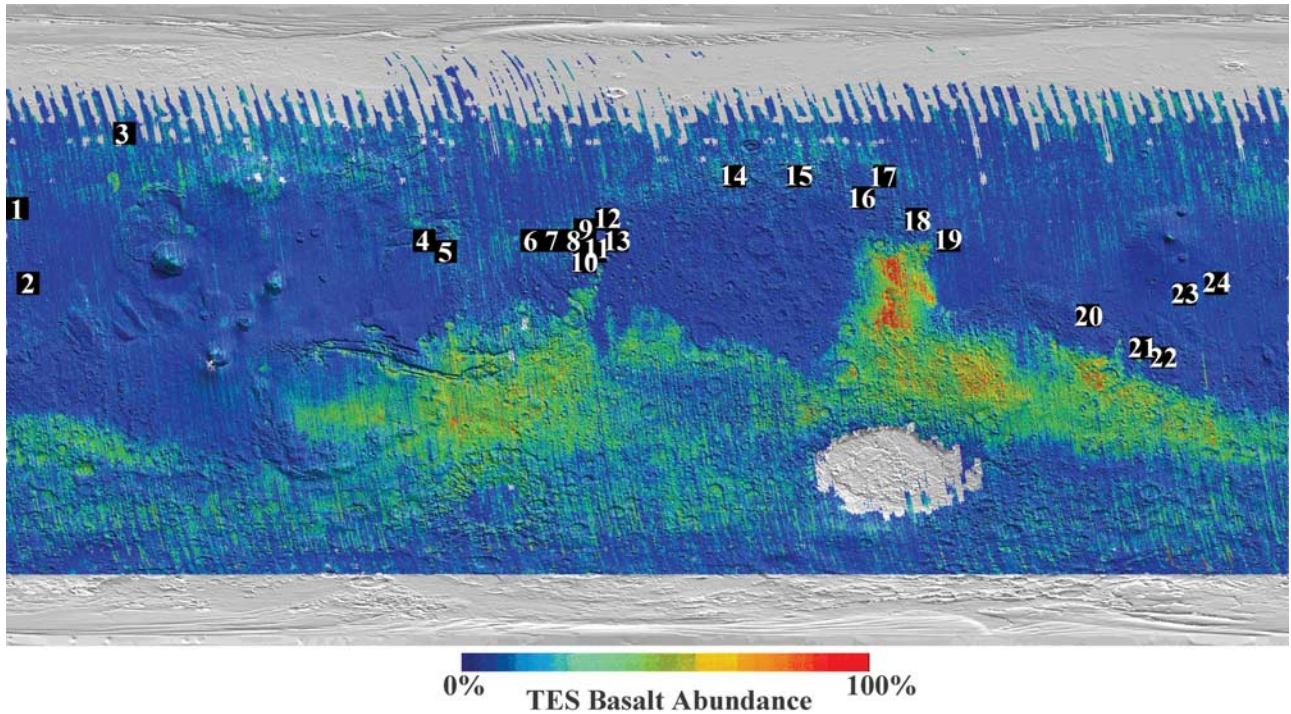


**Figure 5.** Location of small isolated basalt regions identified in this study, superimposed on a combined MOLA shaded-relief map and basalt concentration map (8 ppd,  $\sim 56 \text{ km}^2$  at the equator). All of the regions fall in areas originally mapped as 0–0.40 basalt concentrations in the low-resolution (1 ppd) maps of *Bandfield et al.* [2000a]. The areal extent of most of these regions is less than a  $1^\circ \times 1^\circ$  bin.

any possible compositional deviation from the Syrtis Major type basalt. The averaged effective emissivity spectrum from each basalt region, as well as representative effective emissivity spectra from Syrtis Major and Acidalia Planitia,

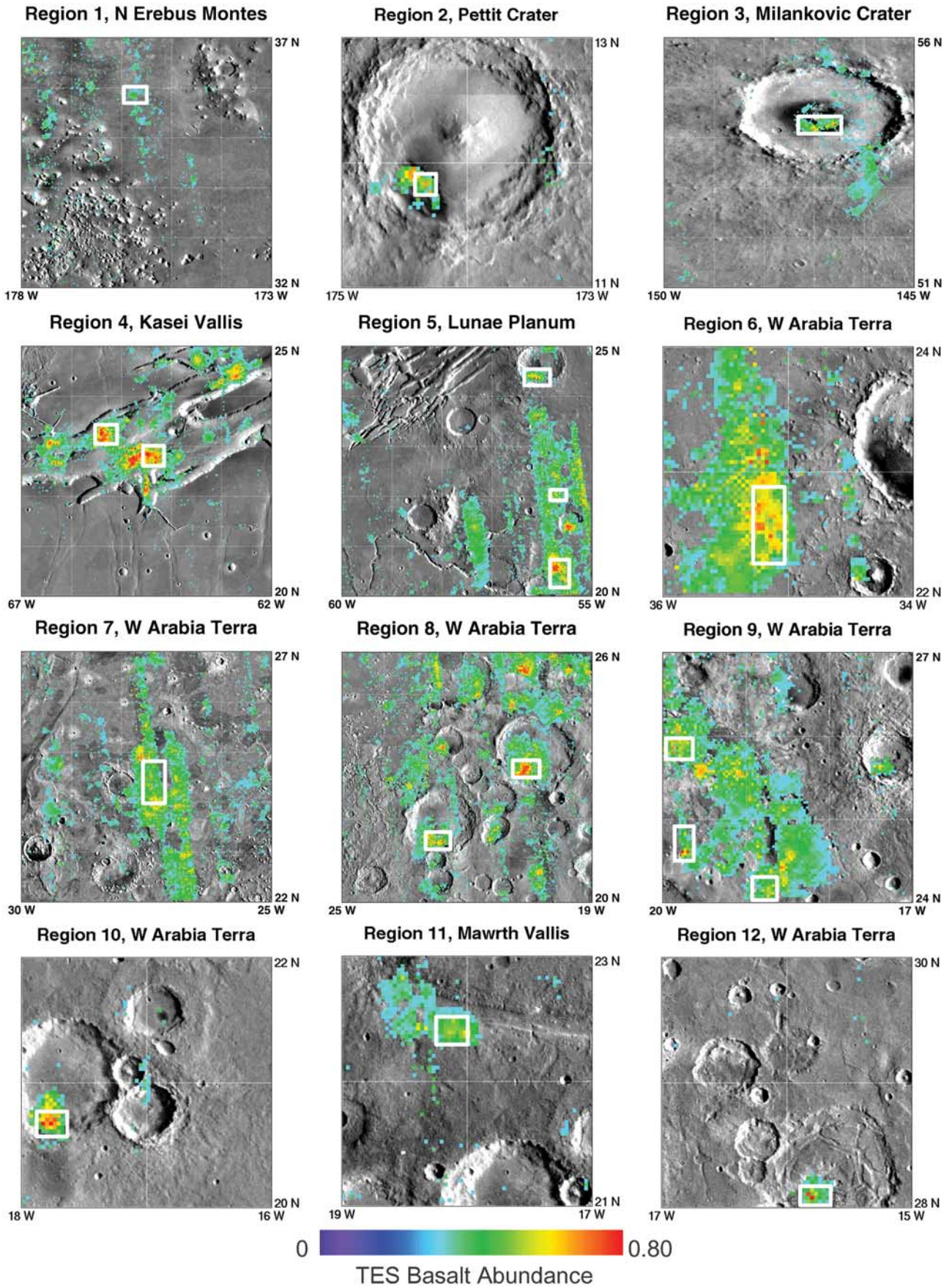
were deconvolved with mineral and atmospheric endmembers (Table 2). Note that this endmember set is different than that used by *Bandfield et al.* [2000a] and therefore gives slightly different results than those given in *Bandfield*

**Table 3.** Basalt Region Locations and Themophysical Characteristics

Region	Coordinates <sup>a</sup>	General Location Name	TES Albedo	Mean Thermal Inertia, $\text{J/m}^2\text{Ks}^{1/2\text{b}}$	Area, $\text{km}^2$
1	35–36N, 175–176W	N Erebus Montes	0.20	218	$\sim 160$
2	11–12N, 174–175W	Pettit Crater	0.12–0.13	224	$\sim 180$
3	54–55N, 146–148W	Milankovic Crater	0.13	354	$\sim 165$
4	22–24N, 64–66W	Kasei Vallis	0.08–0.14	335	$\sim 6500$
5	24–25N, 62–63W	Lunae Planum	0.10–0.16	272	$\sim 6500$
	20–22N, 55–57W				
6	22–23N, 35–36W	W Arabia Terra, Oxia Palus	0.15–0.16	583	$\sim 4890$
7	24–25N, 27–28W	W Arabia Terra, S Acidalia Planitia	0.14–0.15	430	$\sim 3260$
8	21–24N, 20–23W	W Arabia Terra, Oxia Palus	0.08–0.13	473	$\sim 6500$
9	24–26N, 18–20W	Mawrth Vallis, Arabia Terra	0.11–0.15	340	$\sim 4570$
10	20–21N, 17–18W	W Arabia Terra	0.11–0.13	262	$\sim 160$
11	22–23N, 17–19W	Mawrth Vallis, Arabia Terra	0.14	261	$\sim 200$
12	27–29N, 15–17W	W Arabia Terra	0.13–0.17	320	$\sim 140$
13	23–25N, 10–12W	W Arabia Terra	0.14	356	$\sim 160$
14	40–42N, 334–336W	Deuteronilus Mensae	0.12–0.15	255	$\sim 650$
15	41–43N, 315–317W	Moreux Crater	0.10–0.14	248	$\sim 490$
16	36–37N, 300–302W	Protonilus Mensae	0.10–0.13	248	$\sim 1970$
17	42–44N, 293–295W	N Nilosyrtis Mensae	0.14–0.15	298	$\sim 3940$
18	27–29N, 283–285W	W Nilosyrtis Mensae	0.12–0.13	422	$\sim 2840$
19	25–26N, 276–277W	Peridier Crater	0.12–0.17	287	$\sim 250$
20	2–3N, 237–238W	Nepenthes Mensae	0.13	353	$\sim 150$
21	5–7S, 222–224W	Gale Crater & surrounding area	0.11–0.13	355	$\sim 7000$
22	8–9S, 216–218W	Aeolis Mensae	0.15	285	$\sim 900$
23	9–10N, 210–211W	Cerberus	0.10–0.12	305	$\sim 3670$
24	12–14N, 198–200W	Cerberus	0.13	254	$\sim 11000$
	10–12N, 200–202W				

<sup>a</sup>Coordinates which encompass the basalt region.

<sup>b</sup>*Mellon et al.* [2000].



*et al.* [2000a] for the Syrtis Major and Acidalia type surfaces. Sheet silicates (clays and micas) and glass were combined into the same group because of their spectral similarities [see *Bandfield*, 2002].

### 3.2. Characterization of Isolated Basalt Regions

[24] Once the basalt composition was confirmed, other datasets were then used to further characterize these basalt regions. TES thermal inertia and albedo datasets were examined for each region, in an effort to infer a particle size for the basaltic materials [*Kieffer et al.*, 1977; *Presley and Christensen*, 1997; *Presley*, 2002]. High-resolution (256 ppd) mosaics derived from Viking orbiter images were used to determine if the areal distribution of basalt in each region is correlated with landforms or albedo features. For instance, many of the basalt regions correspond to intracrater dark materials [see e.g., *Christensen*, 1983]. In addition, the MGS Mars Orbiter Camera (MOC) database was searched for high-resolution (<5 m/pixel) images that cover the basaltic surface spectra coordinates, in an effort to determine what type of surface corresponds to the detected basaltic signature in each region (such as lava flows or dunes).

## 4. Results

### 4.1. Distribution of Isolated Basalt Regions

[25] Twenty-four isolated basalt regions have been identified between 20°S–60°N, 0–360°W (Figure 5). The areal extent of most of these regions is less than a 1° × 1° bin. All of these regions are located within larger areas that have substantial amounts of surface dust. Table 3 shows the location and thermophysical characteristics of each region, while Figure 6 shows the distribution of basalt for each region, superimposed on high-resolution Viking image mosaics. The majority of the regions are associated with isolated low-albedo areas, typically located on canyon or crater floors. The general geographic locations of the basalt regions are described below.

#### 4.1.1. Arabia Terra (Regions 6–13)

[26] There are few low-albedo surfaces found in Arabia Terra owing to extensive dust cover; intracrater dark materials comprise the majority of low-albedo surfaces in this area. Four of the basalt regions found in Arabia are associated with these surfaces. However there are also high concentrations of basalt along Mawrth Vallis (Regions 9, 11). Two of the basalt regions (Regions 6, 7) are located on the border between western Arabia and southwest Acidalia. One MOC image (Figure 7) was found to cover the exact coordinates of intracrater basalt in Arabia Terra. Small dunes are visible in this image and are probably contributing to the basaltic signature measured with TES in this region. As mentioned above, most of the basalt regions in this study are likely to be derived from the local bedrock, based on the limited transport distance of basaltic sand (Table 1) and the process of sand trapping. Therefore Arabia Terra bedrock is likely to contain basalt. While it

is possible that the intracrater materials are derived from other sources, such as consolidated volcanic ash or impact melt sheets, the regions in this study are similar in composition to large areas of the southern cratered terrain (Surface Type I) [*Bandfield et al.*, 2000a]. The extensive areal coverage of this surface type implies that the composition is related to the crust lithology. Therefore the preferred interpretation for these deposits is that they are also derived from bedrock, rather than localized impact melt sheets or local/regional volcanic ash deposits.

[27] It is important to note that concentrations of andesite (30–65%) are also found in the northwestern part of Mawrth Vallis (Regions 9, 11), as well as the eastern side of Ares Vallis. In addition, andesite, along with basalt concentrations, has been detected in Western Arabia Terra craters and corresponding wind streaks [*Wyatt et al.*, 2001]. It is possible that the andesitic materials in Arabia Terra are locally derived, either from andesite layers exposed in the crater walls [*Wyatt et al.*, 2001], or from andesitic flows at the surface. Another possibility is that the andesitic materials have been transported in from a separate location. The distribution of basalt and andesite in Western Arabia Terra craters suggests that the andesite is finer grained than the basalt in this area [*Wyatt et al.*, 2001]. This could be evidence that the andesitic materials have been transported a greater distance and originated elsewhere.

#### 4.1.2. Lunae Planum/Kasei Vallis (Regions 4–5)

[28] High concentrations of basalt are found in north-eastern Lunae Planum and in Kasei Vallis. The Kasei Vallis basalt corresponds to low-albedo materials on the canyon floor. However, even in the highest resolution MOC images of these dark areas no distinct landforms can be resolved.

#### 4.1.3. Fretted Terrain/Crustal Dichotomy Boundary Zone (Regions 14–22)

[29] The basalt regions in this area are associated with intracrater dark materials, and in between mesas of the fretted terrain. No MOC images were found to correspond exactly with basaltic surfaces.

#### 4.1.4. Northern Lowland Outliers (Regions 1–3, 23–24)

[30] Four regions of significant basalt concentrations are found completely isolated within the northern plains. One is Cerberus (see regions 23–24), a large volcanic plain that is undergoing active aeolian reworking, as evidenced by temporal changes in albedo observed between Mariner 9 [*Chaikin et al.*, 1981] and MGS. There are equally high concentrations of basalt and andesite adjacent to each other, with no difference in thermal inertia values between either composition. The second region is adjacent to Erebus Montes (region 1), located ~2300 km north of the southern cratered terrain. The third is Milankovic Crater (region 3), located ~2800 km north of the cratered terrain and ~900 km northwest of Olympus Mons. The fourth is Petit Crater (region 2), located approximately 1300 km north of the southern cratered terrain. Possible

**Figure 6.** (opposite) Basalt distribution for each of the isolated regions superimposed on high-resolution Viking image mosaics (256 ppd, ~54 m<sup>2</sup> at the equator). The white boxes enclose the approximate locations from which surface spectra were retrieved and averaged. General locations and other characteristics for each region are listed in Table 3.

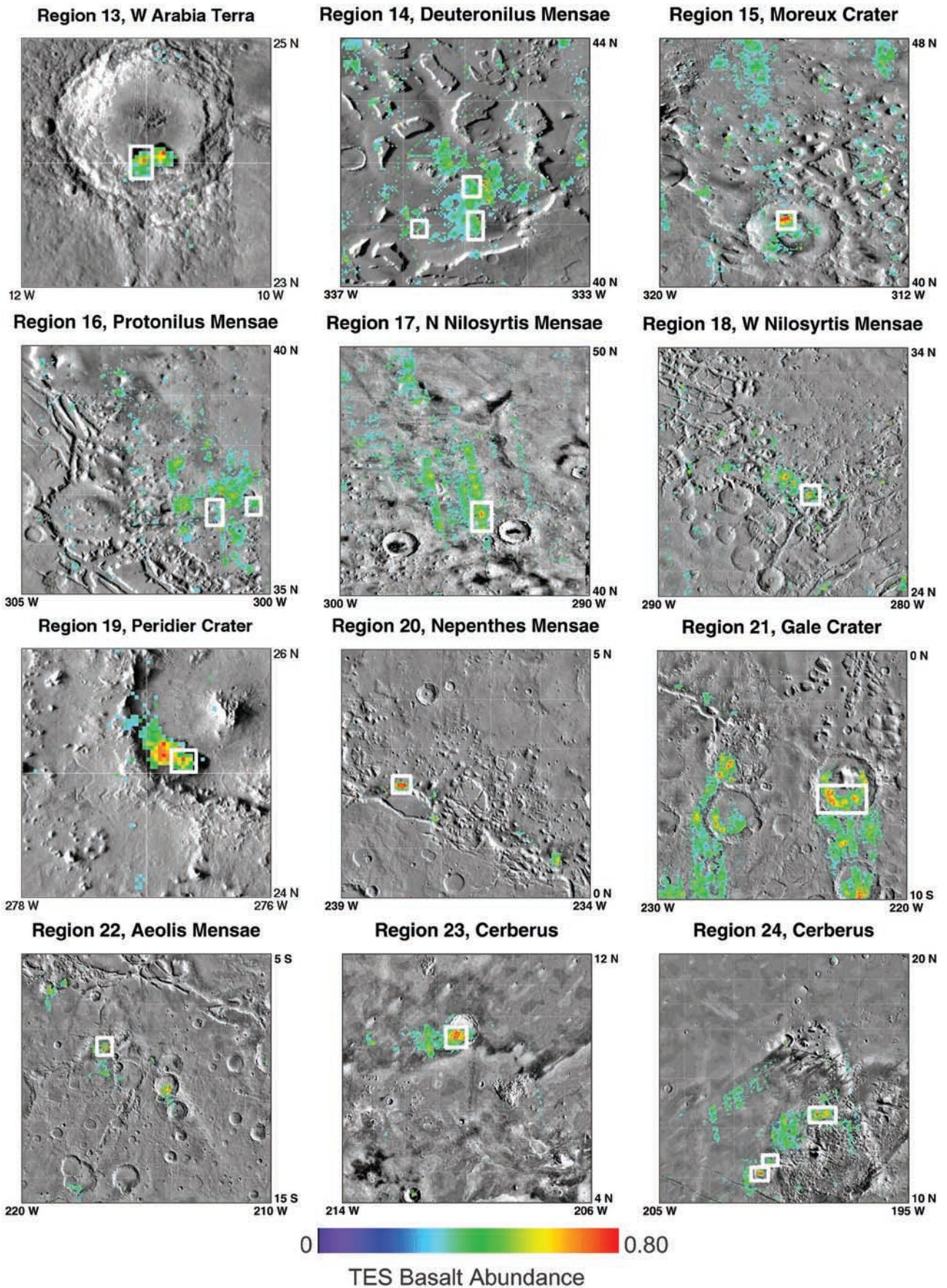
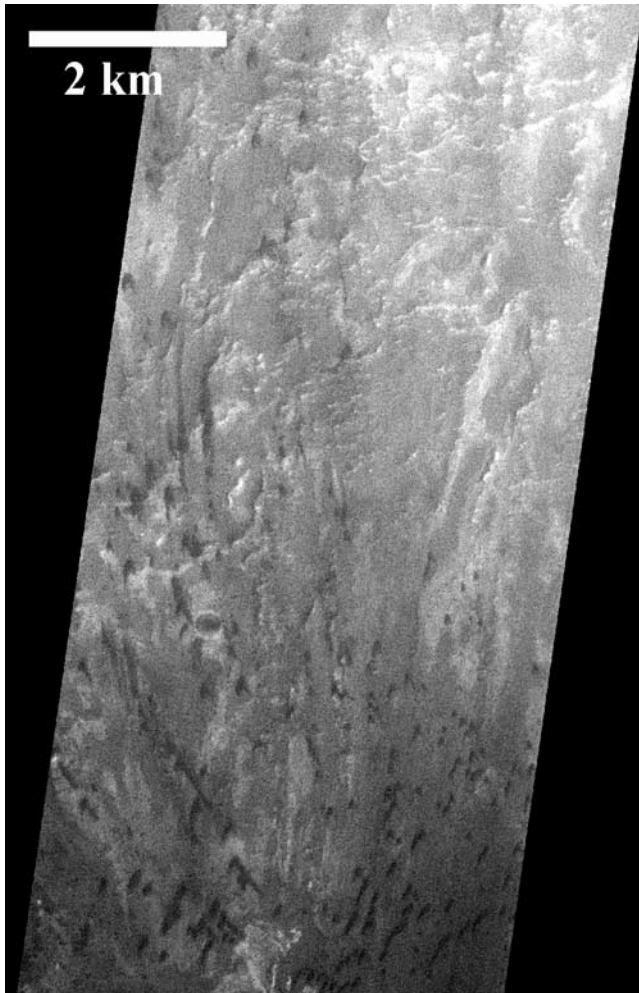


Figure 6. (continued)



**Figure 7.** Southern portion of MOC image SP2-34903 (center coordinates 21.79°N, 22.7°W). The area shown is located within McLaughlin Crater, Western Arabia Terra, Region 8. Small, widely spaced dunes can be resolved.

origins of the basalt found in these outlier regions are discussed in section 5.

#### 4.2. Surface Spectra From Each Isolated Region

[31] Figure 8 shows the averaged surface spectrum from each region. Some of the region spectra have slight deviations either in the depth or location of spectral features, when compared to the Syrtis Major surface spectrum. Shallower spectral feature depth (spectral contrast) can be explained by either a finer particle size than that of Syrtis Major, a thin coating of surface dust, or patches of surface dust that are mixed with the basalt in a checkerboard fashion and detected in the TES field of view. The presence of additional spectral features or the lack of features that are present in the Syrtis type spectra can be attributed to either slight changes in the surface mineralogy, concentrations of andesite mixed in with the basalt or minor atmospheric features that were not completely removed in the deconvolution process. Table 4 shows the modal mineralogy for each representative surface spectrum, compared with that of an average Syrtis Major and Acidalia Planitia surface. Only mineral groups

with abundances commonly  $\geq 10\%$  are shown. For many of the regions, differences in abundances are minor and below the TES detection limit for mineral concentrations ( $< 10\%$ ) [e.g., *Christensen et al.*, 2000a] using current atmospheric correction techniques. Some regions show a decreased abundance of pyroxene and increased amounts of sheet silicates/high-silica glass. The spectral shape that corresponds with these regions, previously described as the “intermediate” surface by *Bandfield et al.* [2000a], could be explained by either a new surface composition that is intermediate between the basaltic and andesitic surface compositions or by concentrations of andesite mixed in with the basalt. It is difficult to determine which explanation is correct; however, the majority of regions with intermediate surfaces are located near the boundary between the basaltic and andesitic compositions. For the regions in this study, it is likely that intermediate surfaces are mixtures of basaltic and andesitic sediments. Thus all of the regions are considered to be composed at least partly of the Syrtis Major-type basalt [*Bandfield et al.*, 2000a] and are probably not local variations in composition.

#### 4.3. Thermophysical Characteristics

[32] All regions have thermal inertia values ( $\sim 225$  to  $> \sim 600$   $\text{J/m}^2\text{Ks}^{1/2}$ ) indicative of particle sizes within the range of fine sand to pebbles ( $\sim 200$  to  $> \sim 15,000$   $\mu\text{m}$ ); (Figure 9). None have values that are consistent with bedrock ( $\sim 2400$   $\text{J/m}^2\text{Ks}^{1/2}$ ) [e.g., *Jakosky*, 1979].

### 5. Discussion

#### 5.1. Distribution of Volcanic Surface Compositions on Mars

[33] Results from this study are consistent with the previous results of *Bandfield et al.* [2000a]. Low-albedo surfaces within the cratered terrain, including Arabia Terra, are composed of basalt to basaltic andesite, while surfaces in the northern smooth plains are composed of basaltic andesite to andesite. The largest areal coverage of andesite concentrations is located in Acidalia Planitia and the rest of the northern plains, but smaller areas of significant andesite concentrations are also distributed throughout the southern cratered terrain. In addition, four isolated regions in the northern hemisphere are at least partially composed of the Syrtis Major-type basalt.

#### 5.2. Local Versus Regional Origin

[34] The effective grain size for these regions ranges from  $\sim 200$   $\mu\text{m}$  to  $> \sim 15,000$   $\mu\text{m}$  (Figure 9). It is important to note that particle size mixtures are likely to be present and that in some cases, measured thermal inertia values could represent a combination of very fine sand ( $< 100$   $\mu\text{m}$ ) and very coarse material (pebble- to cobble-sized) [*Jakosky*, 1979]. In general, low-albedo regions have rock abundances between 6 and 14% [*Christensen*, 1986]. Many of the basalt regions in this study are located in crater and canyon floors, while others are associated with surfaces that are not topographic depressions. The question of whether the basaltic materials in these regions are of local origin (derived from bedrock less than a few hundred kilometers away) or regional origin (derived from bedrock

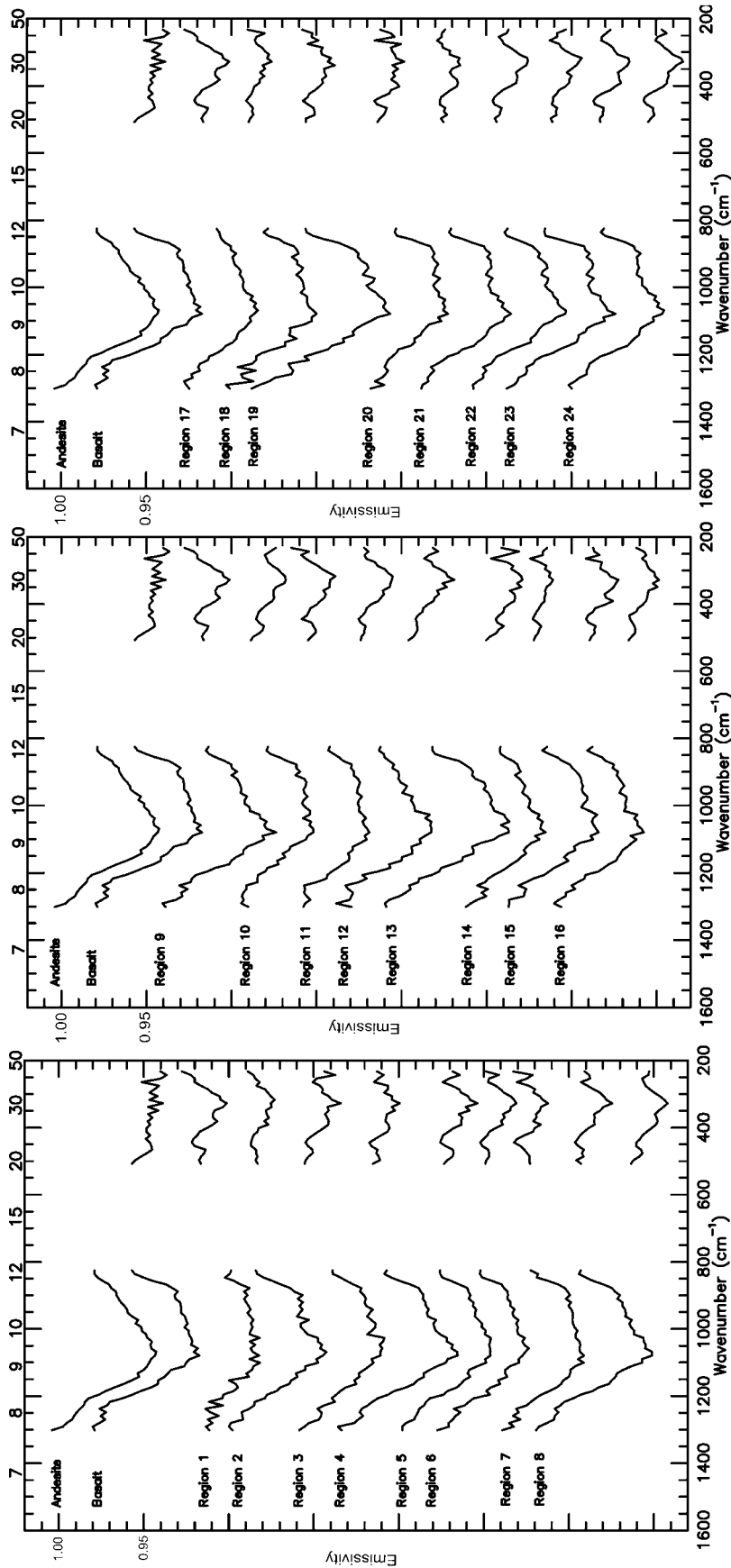


**Figure 8.** The average surface emissivity spectrum for each basalt region, compared with the Acidalia-type surface spectrum (Andesite) and the Syrtis Major-type surface spectrum (Basalt). Spectra are offset for clarity. Anywhere from 6 to 50 surface spectra were used in the average for each region. The coordinates for each surface spectrum used in the average were recorded and used to retrieve thermal inertia and albedo values that correspond with the basalt. The small absorption feature (between  $1025\text{ cm}^{-1}$  and  $1100\text{ cm}^{-1}$ ) that is present in some of the spectra is due to incomplete removal of an atmospheric  $\text{CO}_2$  hot band [Maguire, 1977; Bandfield *et al.*, 2000b, Figure 14] in the surface-atmosphere separation of the effective emissivity spectra. Thus although it is not a true surface absorption, it is added to the surface spectral component in the atmospheric removal process.

**Table 4.** Deconvolution Results for Regions 1–24 Compared With Syrtis Major and Acidalia Surfaces

Mineral Group/Lithologic Endmember	1	2	3 <sup>c</sup>	4	5	6	7	8	9	10	11	12 <sup>d</sup>	13	14	15	16	17	18	19	20	21	22	23	24	Syrtis Major <sup>e</sup>	Acidalia <sup>c</sup>	
<i>Mineral Areal Abundances for Regions 1–24 Compared With Syrtis Major and Acidalia Regional Surfaces, %</i>																											
Feldspar	44	46	30	32	33	40	42	40	43	41	50	28	38	37	45	32	38	37	38	36	35	38	35	42	42	35	
Pyroxene	23	31	31	26	19	26	29	29	17	26	24	18	20	34	25	19	16	32	26	32	26	22	25	26	33	(9) <sup>f</sup>	
Sheet Silicates/Glass	18	15	13	28	35	21	10	22	27	19	11	37	31	12	18	33	30	18	19	18	22	23	20	21	15	42	
Other <sup>b</sup>	15	9	26	14	13	13	18	10	11	13	15	16	10	17	11	16	17	12	17	13	18	17	18	11	10	14	
Blackbody <sup>g</sup>	68	50	56	38	42	51	50	32	43	53	52	31	27	57	44	49	57	43	31	45	42	44	38	52	30	38	
<i>Basalt and Andesite Abundances<sup>h</sup> for Regions 1–24</i>																											
Basalt Abundance	47	51	52	56	57	66	52	59	40	69	56	40	57	43	63	42	33	61	63	64	56	53	66	52	95	26	
Andesite Abundance	0	35	20	47	32	7	22	47	60	0	6	35	60	14	20	36	38	13	57	24	26	38	26	28	21	74	

<sup>a</sup>Mineral percentages from the deconvolution output are normalized to exclude atmospheric and blackbody components, after *Bandfield et al.* [2000a]. Abundances are rounded to the nearest whole number. This is why mineral groups do not sum to exactly 100%.

<sup>b</sup>Includes the following mineral groups: hematite, sulfate, carbonate, olivine, quartz, and phosphate. Abundances from these individual mineral groups are present below the detection limit (<10%), except where indicated.

<sup>c</sup>Deconvolution results for this region also yields 11% carbonate, in addition to feldspar, pyroxene, and sheet silicates/glass abundances.

<sup>d</sup>Deconvolution results for this region also yields 11% sulfate, in addition to feldspar, pyroxene, and sheet silicates/glass abundances.

<sup>e</sup>Examples given are for typical Syrtis Major and Acidalia regional surfaces.

<sup>f</sup>Deconvolution results for a regional Acidalia surface yields 9% pyroxene, which is slightly below the detection limit.

<sup>g</sup>Blackbody abundance is from deconvolution results of atmospherically corrected spectra.

<sup>h</sup>For comparison, results from the deconvolution using three surface endmembers (Syrtis Major type surface, Acidalia type surface, hematite surface), four atmospheric endmembers, and blackbody are shown. Abundances are not normalized to exclude the blackbody and atmospheric components to compare with basalt abundance maps in Figure 6.

more than several hundreds of kilometers away) is discussed below.

**5.2.1. Intracrater Deposits/Canyon Floors**

[35] The thermal inertia of the basalt regions associated with crater/canyon floors ranges from ~250 to 600 J/m<sup>2</sup>Ks<sup>1/2</sup>, which corresponds to an effective particle size of ~280 to ~15,000 μm [*Presley and Christensen*, 1997]. Most of the regions associated with topographic depressions have thermal inertia values >~350 J/m<sup>2</sup>Ks<sup>1/2</sup> (effective particle size >~1200 μm) (Figure 9), which is the average thermal inertia of dune sand on Mars [*Edgett and Christensen*, 1991]. This observation has also been noted by *Christensen* [1983], who suggested that the majority of intracrater deposits with a

thermal inertia >~350 J/m<sup>2</sup>Ks<sup>1/2</sup> are likely to be low, broad zibar dunes or lag deposits, formed by grains that can be transported into but not out of the craters. It is also probable that there is impact-related sand and rocky material present. Most importantly, because of the large number of craters in the southern highlands, it seems difficult for coarse sand grains to travel far without becoming trapped. In summary, basaltic materials found in topographic depressions such as crater floors are interpreted to be derived from the nearby bedrock.

**5.2.2. Other Low-Albedo Surfaces**

[36] Other basalt regions in this study are not associated with steeply enclosed topographic depressions, such as in

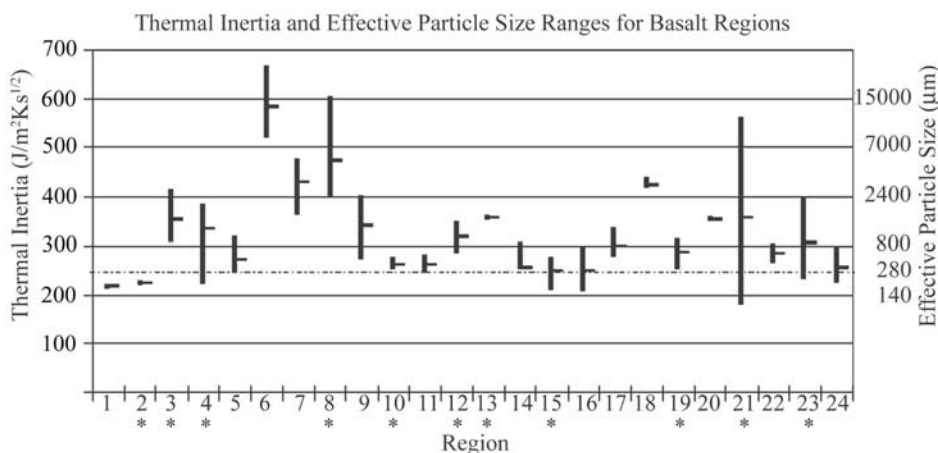


**Figure 9.** Thermal inertia and effective particle size ranges for each region. Horizontal tick marks show the mean values. The thermal inertia values were taken from the exact coordinates recorded for each surface spectrum that was used in the average surface spectrum for each region (see Figure 8). Effective particle sizes are approximated by using the thermal conductivity values from Figures 12 and 14 of *Presley and Christensen* [1997], for a Martian atmosphere of 5 torr (~6.7 mbar) and a density and specific heat product of 0.24 cal<sup>o</sup>K<sup>-1</sup>cm<sup>-3</sup>. Asterisks indicate basalt regions associated with intracrater deposits or canyon floors.

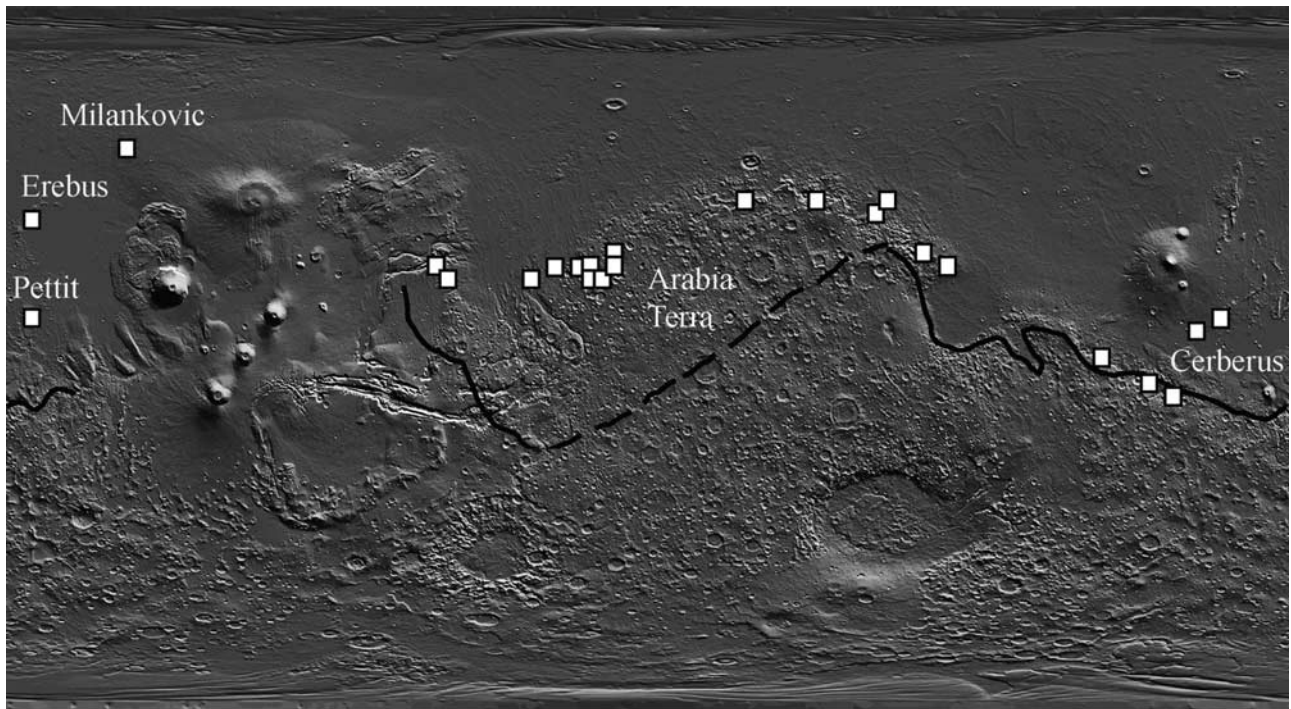


**Figure 10.** The isolated basalt region locations from Figure 5, superimposed on a MOLA shaded relief map (16 ppd). Areas north of the black line generally have a crustal thickness less than 40 km, as shown by Zuber *et al.* [2000]; this line is a general approximation of the crustal thickness boundary described in Zuber *et al.* [2000]. Arabia Terra is the large region in the center, which has the crustal thickness of the smooth northern plains but the geomorphology of the cratered terrain.

Lunae Planum (Region 5) and Mawrth Vallis (Regions 9, 11). Thermal inertia values for most of these regions range from  $\sim 225$  to  $\sim 470 \text{ J/m}^2\text{Ks}^{1/2}$  (effective particle size  $\sim 200$  to  $\sim 5000 \mu\text{m}$  [Presley and Christensen, 1997]). Region 6 has an effective particle size  $>15000 \mu\text{m}$ . Compared with the intracrater basaltic materials, overall these regions have slightly lower effective particle sizes and therefore may have farther transport distances. However, for most of the regions, these estimated distances are still within the range of a local origin. In addition, low-albedo surfaces ( $<0.18$ ) commonly have rock abundances of 6–14% and may be as high as 14–28% [Christensen, 1986]. It is likely that basaltic materials in these regions are locally derived. Regions with the lowest thermal inertia values ( $\sim 200 \text{ J/m}^2\text{Ks}^{1/2}$ , Regions 1–2) could have longer transport distances and a regional origin cannot be ruled out for these two areas.

### 5.3. Association of the Basaltic Composition With Surface Geology

[37] Figure 10 shows the location of the basalt regions, superimposed on a MOLA shaded relief map. This map shows that the basaltic surface composition appears to be closely associated with the cratered terrain morphology. All but four of the regions (the two regions in Cerberus, regions 23 and 24, are considered one region) are located within the cratered terrain and along the cratered terrain morphologic boundary. With these four exceptions, there are no significant ( $>\sim 30\%$  surface cover) concentrations of basalt  $>\sim 400 \text{ km}^2$  in size within the northern smooth plains. For this work, a “significant” concentration of basalt was consid-

ered to be 30%. In the 32 ppd basalt abundance maps, all spatially coherent elevated basalt concentrations ( $>10\%$  surface cover) were examined. However, elevated basalt concentrations that appeared to be associated only with individual orbit tracks were not examined. Concentrations that follow the orbit track spatial pattern are likely a result of relatively high noise levels or increased atmospheric water ice and dust loadings, rather than representing a real surface concentration. In general, concentration values that are associated with this occurrence are  $<30\%$ ; consequently, this was the value chosen to represent a “significant” concentration. “Significant concentration” values for a basalt abundance map should not be confused with the mineral detection limit, which is  $\sim 10\text{--}15\%$  for deconvolution of individual spectra.

### 5.4. Association of the Basaltic Composition With Crustal Thickness

[38] Figure 10 also shows the approximate location of the crustal thickness boundary of Zuber *et al.* [2000]. As discussed in section 1, Arabia Terra exhibits cratered terrain morphology but has a relatively thin crust like the northern plains. Eight of the basalt regions in this study are located in the Arabia Terra province (Regions 6–13). It is likely that these basaltic materials ( $\sim 400$  to  $>\sim 15,000 \mu\text{m}$ ) are derived from Arabia Terra bedrock because they are estimated to have been transported less than a few hundred kilometers (Table 1). Therefore Arabia Terra bedrock is at least partially composed of basalt. The areal distribution of the basaltic surface composition in this region extends as far as  $\sim 3000 \text{ km}$  north of the approximate crustal thickness

boundary, indicating that the global distribution of the basaltic surface composition is not correlated with crustal thickness in this region.

## 5.5. Origin of Basaltic Outliers in the Northern Lowlands

### 5.5.1. Cerberus (Regions 23–24)

[39] Cerberus, located  $\sim 1500$  km north of the cratered terrain, has high concentrations of basalt (>30% up to 100%) and corresponding thermal inertia values of  $\sim 250\text{--}300$  J/m<sup>2</sup>Ks<sup>1/2</sup> ( $\sim 280\text{--}800$   $\mu\text{m}$  effective particle size). It should be noted that there are equally high concentrations of andesite intermixed with the basalt throughout the region. Neither composition appears associated with a unique thermal inertia range or a particular landform morphology. Although it is difficult to determine unequivocally the source of the basalt in Cerberus, there are three scenarios: (1) the source is the Elysium province (this is difficult to confirm with TES because of extensive dust cover); (2) it is derived from a local eruption within the Cerberus region (this may be supported by the results of Plescia [1990], who described the Cerberus plains as Amazonian flood lavas and mapped nine features interpreted to be volcanic vents in Western Cerberus), or (3) basalt has been eroded from the knobby terrain to the immediate southeast. One previous interpretation for the knobby terrain unit is that it is remnant cratered terrain material [e.g., Carr, 1981, p. 73; Greeley and Guest, 1987; Plescia, 1990]. (In other areas such as Acidalia Planitia and Isidis Planitia, parts of the knobby terrain unit have been interpreted as pseudocraters [Frey et al., 1979; Frey and Jarosewich, 1982; Greeley and Fagents, 2001].) If the knobby terrain is remnant cratered terrain and the basaltic surface composition is associated with the cratered terrain, it follows that some basaltic material may have been eroded from the remnants and deposited in Cerberus. Although dominant wind directions in Cerberus are currently from the northeast, it is possible that paleowind directions were from the southeast. As with the Elysium province, the knobby terrain itself is too dust-covered to determine a surface composition; perhaps the increased spatial resolution of future infrared experiments such as the Thermal Emission Imaging System aboard the 2001 Mars Odyssey spacecraft will help to determine the composition of these areas.

### 5.5.2. North Erebus Montes (Region 1)

[40] A second basalt outlier is located adjacent to Erebus Montes (35°N, 175°W). This region has moderate basalt concentrations and an average thermal inertia of  $\sim 225$  J/m<sup>2</sup>Ks<sup>1/2</sup> (effective particle size of  $\sim 200$   $\mu\text{m}$ ). Erebus Montes is mapped as undivided units (Hnu), with one interpretation that these units are erosional remnants of cratered terrain [Scott and Tanaka, 1986]. Possibilities for the origin of the basalt in this region are (1) the basalt is derived from Erebus Montes cratered terrain remnants (again, these remnants are too dusty to verify a basaltic composition), or (2) it is derived from a local basalt flow. The apparent absence of volcanic vents or constructs make this latter suggestion is less likely.

### 5.5.3. Milankovic Crater (Region 3)

[41] The third basalt outlier is located on the floor of Milankovic crater (54°N, 147°W), approximately 900 km northwest of Olympus Mons. The basalt concentration is

significantly lower than adjacent andesite concentrations; the average thermal inertia of the basalt is  $\sim 350$  J/m<sup>2</sup>Ks<sup>1/2</sup> ( $\sim 1200$   $\mu\text{m}$ ). At  $\sim 2800$  km north of the cratered terrain, Milankovic Crater is well beyond the estimated maximum transport distance (Table 1). Thus it is necessary to hypothesize other possible sources. Three suggestions are offered here: (1) the source area is the Tharsis province (extensive dust deposits make this difficult to confirm with remote spectral measurements); (2) it is derived from a local basalt flow (the lack of any visible volcanic constructs or vents nearby make this explanation less likely); or (3) the andesite composition in the northern smooth plains is relatively thin, and basalt was excavated from beneath during impact.

[42] The idea that an impactor may have punched through a thin andesite layer is supported by recent MOLA observations of buried impact basins in the northern hemisphere. The existence of these basins led Frey et al. [2001a] to conclude that the resurfacing materials in the northern smooth plains are probably only a thin layer. Milankovic is one of the few large-diameter (> $\sim 40$  km) craters in the northern smooth plains; other large-diameter northern plains craters have been examined in an initial effort to look for a possible correlation between basalt presence and crater depth. Preliminary results show that there are other craters that have even greater depths but with high andesite concentrations and no detectable basalt. One explanation for this could be that the northern lowland materials are of variable thickness [Frey et al., 2001b]; another possibility is that exposed basaltic materials could have been resurfaced by later andesite flows. Further study is needed to investigate the potential presence of basalt beneath an andesitic cover.

### 5.5.4. Pettit Crater (Region 2)

[43] The fourth basalt outlier is in Pettit Crater (12°N, 174°W). High concentrations of both basalt (30%–80%) and andesite (30%–90%) are present here in individual spectra; however overall the areal coverage of andesite is much greater. Although Pettit is  $\sim 1300$  km north of the southern cratered terrain, it is located within the knobby terrain that has been suggested to be erosional remnants of the cratered terrain [e.g., Carr, 1981, p.73; Greeley and Guest, 1987; Plescia, 1990]. It is possible that a small amount of basaltic material has been eroded from the cratered terrain remnants and deposited in Pettit Crater, or, as suggested for Milankovic Crater, basaltic materials may have been excavated from beneath during the impact event that formed the crater. A third explanation could be a local basalt flow near Pettit crater, although the lack of any visible volcanic constructs makes this suggestion unlikely. Although their present locations within the crater may not necessarily reflect their origin, it is interesting to note that basaltic materials in Milankovic crater are clustered around the central peak (supporting an impact-excavation origin), while Pettit basaltic material is concentrated in the topographically lowest part of the crater (supporting an erosion and deposition origin).

## 5.6. Implications

[44] The apparent association of the basaltic surface composition with cratered terrain materials indicates that widespread basaltic volcanism of the Syrtis Major-type composition was restricted to Mars' earlier past and is old

relative to the andesitic surfaces in the northern smooth plains. The basaltic outliers in the northern plains may represent local basalt flows that occurred later than the time of formation for the cratered terrain basalt. However, it is important to note that the origin for the basalt in all of these outliers can also be explained by either erosion of cratered terrain remnants (knobby terrain) or impact through a thin andesite layer to expose underlying older basalt. Thus it is possible that all basaltic bedrock from which basaltic sand originated is relatively old (Noachian to early Hesperian).

[45] Zuber *et al.* [2000] hypothesized that Arabia Terra may be an area of exposed northern smooth plains basement. The fact that Arabia Terra is at least partially basaltic supports this hypothesis, in that the extent of the basaltic surface composition does not terminate with the crustal thickness boundary but rather it extends farther north, at least as far as the cratered terrain boundary in Arabia Terra. It is possible that the distribution of cratered terrain basalt continues north into the lowlands, beneath an andesitic resurfacing layer.

[46] Results from this work indicate that the relative areal distributions of basalt and andesite are related to a temporal process, rather than being controlled by spatial means. This further indicates that the topographic difference between the northern lowlands and southern highlands and the formational mechanism for the crustal dichotomy are probably not related to spatial differences in crustal density, as suggested by previous authors [e.g., Hartmann, 1973a; Mutch *et al.*, 1976, p.210].

## 6. Conclusion

[47] From this work, the following conclusions can be made:

[48] 1. With four exceptions, there are no significant concentrations (>30% surface cover) of Syrtis Major-type basalt in the northern plains greater than  $\sim 400 \text{ km}^2$ .

[49] 2. The compositional dichotomy is closely associated with the morphologic dichotomy, but is not correlated as well with crustal thickness. The cratered terrain is known to be older than the northern smooth plains, because of its higher crater density [e.g., Hartmann, 1973b]. Thus, it appears that basaltic volcanism, for the most part, occurred earlier in Mars' volcanic history, and was later followed by a period of andesitic volcanism that resurfaced much of the northern lowlands. This is consistent with the previous conclusions of Bandfield *et al.* [2000a].

[50] 3. Basaltic material in Cerberus (Regions 23–24) may have originated from the knobby terrain, or may have been eroded from the Elysium Province lavas or may represent a local basalt flow. The basalt adjacent to Erebus Montes (Region 1) is most likely derived from Erebus Montes, which has been interpreted as remnants of highland plateau terrain [Scott and Tanaka, 1986]. Milankovic Crater (Region 3) may represent a local basalt flow, an area of deposition from Tharsis volcanics, or exposed basalt from the impact event to form the crater. Lastly, basaltic material in Pettit Crater (Region 2) may have been derived from the surrounding knobby terrain, or from impact excavation, as suggested for Milankovic crater.

[51] 4. The distribution of basaltic and andesitic compositions is likely to be related to a change in volcanism

through time, rather than controlled by spatial location. This observed distribution implies a stratigraphic relationship with younger andesitic smooth plains overlying the ancient basaltic cratered terrain.

[52] **Acknowledgments.** We would like to acknowledge two anonymous reviewers for their valuable comments and suggestions. Thanks to Josh Bandfield and Michael Kraft for their careful reviews, which led to significant improvement of this manuscript. Timothy Glotch and Amy Knudson also provided helpful reviews of the earliest version of this paper. We would also like to acknowledge Malin Space Science Systems for use of the MGS MOC images. Finally we would like to thank the TES Engineering, Data Processing, and Software teams for all of their outstanding efforts and support.

## References

- Anderson, F. S., R. Greeley, P. Xu, E. Lo, D. G. Blumberg, R. M. Haberle, and J. R. Murphy, Assessing the Martian surface distribution of Aeolian sand using a Mars general circulation model, *J. Geophys. Res.*, *104*, 18,991–19,002, 1999.
- Bandfield, J. L., Global mineral distributions on Mars, *J. Geophys. Res.*, *107*(E6), 5042, doi:10.1029/2001JE001510, 2002.
- Bandfield, J. L., V. E. Hamilton, and P. R. Christensen, A global view of Martian surface compositions from MGS-TES, *Science*, *287*, 1626–1630, 2000a.
- Bandfield, J. L., P. R. Christensen, and M. D. Smith, Spectral data set factor analysis and end-member recovery: Application to analysis of Martian atmospheric particulates, *J. Geophys. Res.*, *105*, 9573–9587, 2000b.
- Bandfield, J. L., K. S. Edgett, and P. R. Christensen, Spectroscopic study of the Moses Lake dune field, Washington: Determination of compositional distributions and source lithologies, *J. Geophys. Res.*, *107*(E11), 5092, doi:10.1029/2000JE001469, 2002.
- Bell, J. F., M. J. Wolff, P. B. James, R. T. Clancy, S. W. Lee, and L. J. Martin, Mars surface mineralogy from Hubble Space Telescope imaging during 1994–1995: Observations, calibration, and initial results, *J. Geophys. Res.*, *102*, 9109–9123, 1997.
- Brückner, J., G. Dreibus, R. Rieder, and H. Wänke, Revised data of the Mars Pathfinder Alpha Proton X-Ray Spectrometer: Geochemical behavior of major and minor Elements (abstract 1293) [CD-ROM], *Lunar Planet. Space Sci.*, *XXXII*, 2001.
- Carmichael, I. S. E., The petrology of Thingmuli, a Tertiary volcano in eastern Iceland, *J. Petrol.*, *5*, 435–460, 1964.
- Carr, M. H., Volcanism on Mars, *J. Geophys. Res.*, *78*, 4049–4062, 1973.
- Carr, M. H., *The Surface of Mars*, 232 pp., Yale Univ. Press, New Haven, Conn., 1981.
- Chaikin, A. L., T. A. Maxwell, and F. El-Baz, Temporal changes in the Cerberus Region of Mars: Mariner 9 and Viking comparisons, *Icarus*, *45*, 167–178, 1981.
- Christensen, P. R., Eolian intracrater deposits on Mars: Physical properties and global distribution, *Icarus*, *56*, 496–518, 1983.
- Christensen, P. R., The spatial distribution of rocks on Mars, *Icarus*, *68*, 217–238, 1986.
- Christensen, P. R., et al., Thermal Emission Spectrometer Experiment: Mars Observer Mission, *J. Geophys. Res.*, *97*, 7719–7734, 1992.
- Christensen, P. R., J. L. Bandfield, M. D. Smith, V. E. Hamilton, and R. N. Clark, Identification of a basaltic component on the Martian surface from Thermal Emission Spectrometer data, *J. Geophys. Res.*, *105*, 9609–9621, 2000a.
- Christensen, P. R., et al., Detection of crystalline hematite mineralization on Mars by the Thermal Emission Spectrometer: Evidence for near-surface water, *J. Geophys. Res.*, *105*, 9623–9642, 2000b.
- Christensen, P. R., J. L. Bandfield, V. E. Hamilton, D. A. Howard, M. D. Lane, J. L. Piatek, S. W. Ruff, and W. L. Stefanov, A thermal emission spectral library of rock-forming minerals, *J. Geophys. Res.*, *105*, 9735–9739, 2000c.
- Christensen, P. R., et al., The Mars Global Surveyor Thermal Emission Spectrometer Experiment: Investigation description and surface science results, *J. Geophys. Res.*, *106*, 23,823–23,871, 2001a.
- Christensen, P. R., R. V. Morris, M. D. Lane, J. L. Bandfield, and M. C. Malin, Global mapping of Martian hematite mineral deposits: Remnants of water-driven processes on early Mars, *J. Geophys. Res.*, *106*, 23,873–23,885, 2001b.
- Edgett, K. S., and P. R. Christensen, The particle size of Martian aeolian dunes, *J. Geophys. Res.*, *96*, 22,765–22,776, 1991.
- Feeley, K. C., and P. R. Christensen, Quantitative compositional analysis using thermal emission spectroscopy: Application to igneous and metamorphic rocks, *J. Geophys. Res.*, *104*, 24,195–24,210, 1999.

- Foley, C. N., T. E. Economou, W. Dietrich, and R. N. Clayton, Chemical composition of Martian soil and rocks: Comparison of the results from the alpha, proton, and X-ray modes of the Mars Pathfinder alpha-proton X-ray spectrometer, *Meteoritics Planet. Sci.*, 35, A55–A56, 2000.
- Frey, H., and M. Jarosewich, Subkilometer Martian volcanoes: Properties and possible terrestrial analogs, *J. Geophys. Res.*, 87, 9867–9879, 1982.
- Frey, H., B. L. Lowry, and S. A. Chose, Pseudocraters on Mars, *J. Geophys. Res.*, 84, 8075–8086, 1979.
- Frey, H. V., K. M. Shockey, E. L. Frey, J. H. Roark, and S. E. H. Sakimoto, A very large population of likely buried impact basins in the northern lowlands of Mars revealed by MOLA data (abstract 1680) [CD-ROM], *Lunar Planet. Sci.*, XXXII, 2001a.
- Frey, H. V., G. J. Hohner, A. Wernecke, J. H. Roark, and S. E. Sakimoto, Buried impact basins as constraints on the thickness of ridged plains and northern lowland plains on Mars (abstract P42A-0551), *Eos Trans. AGU*, 82, Fall Meet. Suppl., 2001b.
- Gill, J., *Orogenic Andesites and Plate Tectonics*, 390 pp., Springer-Verlag, New York, 1981.
- Gillespie, A. R., Spectral mixture analysis of multispectral thermal infrared images, *Remote Sens. Environ.*, 42, 137–145, 1992.
- Greeley, R., and S. A. Fagents, Icelandic pseudocraters as analogs to some volcanic cones on Mars, *J. Geophys. Res.*, 106, 20,527–20,546, 2001.
- Greeley, R., and J. E. Guest, Geologic map of the eastern equatorial region of Mars, *U.S. Geol. Surv. Misc. Invest. Map, I-1802-B*, scale 1:15,000,000, 1987.
- Greeley, R., and J. D. Iversen, *Wind as a Geological Process*, 333 pp., Cambridge Univ. Press, New York, 1985.
- Greeley, R., and M. D. Kraft, Survivability of aggregate sands on Mars (abstract 1839) [CD-ROM], *Lunar Planet. Space Sci.*, XXXII, 2001.
- Greeley, R., R. Leach, B. White, J. Iversen, and J. Pollack, Threshold windspeeds for sand on Mars: Wind tunnel simulations, *Geophys. Res. Lett.*, 7, 121–124, 1980.
- Hamilton, V. E., and P. R. Christensen, Determining the modal mineralogy of mafic and ultramafic igneous rocks using thermal emission spectroscopy, *J. Geophys. Res.*, 105, 9717–9733, 2000.
- Hamilton, V. E., M. B. Wyatt, H. Y. McSween Jr., and P. R. Christensen, Analysis of terrestrial and Martian volcanic compositions using thermal emission spectroscopy, 2, Application to martian surface spectra from the Mars Global Surveyor Thermal Emission Spectrometer, *J. Geophys. Res.*, 106, 14,733–14,746, 2001a.
- Hamilton, V. E., P. R. Christensen, H. Y. McSween Jr., R. N. Clark, and T. M. Hoefen, Spectral variations in MGS TES data of Nili Fossae: A possible source region for SNC meteorites on Mars? (abstract 2184) [CD-ROM], *Lunar Planet. Space Sci.*, XXXII, 2001b.
- Hamilton, V. E., P. R. Christensen, and J. L. Bandfield, Intermediate volcanism vs. aqueous alteration on Mars (communication arising), *Nature*, 421, 711–712, 2002.
- Hartmann, W. K., Martian surface and crust: Review and synthesis, *Icarus*, 19, 550–575, 1973a.
- Hartmann, W. K., Martian cratering, 4, Mariner 9 initial analysis of cratering chronology, *J. Geophys. Res.*, 78, 4096–4116, 1973b.
- Head, J. W., III, M. A. Kreslavsky, and S. Pratt, Northern lowlands of Mars: Evidence for widespread volcanic flooding and tectonic deformation in the Hesperian Period, *J. Geophys. Res.*, 107(E1), 5001, doi:10.1029/2000JE001438, 2002.
- Hoefen, T. M., R. N. Clark, J. C. Pearl, and M. D. Smith, Unique Spectral features in Mars Global Surveyor Thermal Emission Spectra: Implications for surface mineralogy in Nili Fossae (abstract 62.03), *Bull. Am. Astron. Soc.*, 32(1118), 2000.
- Iversen, J. D., J. B. Pollack, R. Greeley, and B. R. White, Saltation threshold on Mars: The effect of interparticle force, surface roughness, and low atmospheric density, *Icarus*, 29, 381–393, 1976.
- Jakosky, B. M., The effects of nonideal surfaces on the derived thermal properties of Mars, *J. Geophys. Res.*, 84, 8252–8262, 1979.
- Kieffer, H. H., T. Z. Martin, A. B. Peterfreund, B. M. Jakosky, E. D. Miner, and F. D. Palluconi, Thermal and albedo mapping of Mars during the Viking primary mission, *J. Geophys. Res.*, 82, 4249–4291, 1977.
- Krinsley, D., and R. Greeley, Individual particles and Martian aeolian action—A review, *Sediment. Geol.*, 47, 167–189, 1986.
- Krinsley, D., R. Greeley, and J. B. Pollack, Abrasion of windblown particles on Mars—erosion of quartz and basaltic sand under simulated Martian conditions, *Icarus*, 39, 364–384, 1979.
- Maguire, W. C., Martian isotopic ratios and upper limits for possible minor constituents as derived from Mariner 9 infrared spectrometer data, *Icarus*, 32, 85–97, 1977.
- Masursky, H., An overview of geological results from Mariner 9, *J. Geophys. Res.*, 78, 4009–4030, 1973.
- Mellon, M. T., B. M. Jakosky, H. H. Kieffer, and P. R. Christensen, High-resolution thermal inertia mapping from the Mars Global Surveyor Thermal Emission Spectrometer, *Icarus*, 148, 437–455, 2000.
- Minitti, M. E., J. F. Mustard, and M. J. Rutherford, Effects of glass content and oxidation on the spectra of SNC-like basalts: Applications to Mars remote sensing, *J. Geophys. Res.*, 107(E5), 5030, doi:10.1029/2001JE001518, 2002.
- Morris, R. V., et al., Acid sulfate alteration products of a tholeiitic basalt: Implications for interpretation of Martian thermal emission spectra (abstract 214) [CD-ROM], *Lunar Planet. Sci.*, XXXI, 2000.
- Mutch, T. A., R. E. Arvidson, J. W. Head III, K. L. Jones, and R. S. Saunders, *The Geology of Mars*, 400 pp., Princeton Univ. Press, Princeton, N. J., 1976.
- Parker, T. J., D. S. Gorsline, R. S. Saunders, D. C. Pieri, and D. M. Schneeberger, Coastal geomorphology of the Martian Northern Plains, *J. Geophys. Res.*, 98, 11,061–11,078, 1993.
- Plescia, J. B., Recent flood lavas in the Elysium region of Mars, *Icarus*, 88, 465–490, 1990.
- Presley, M. A., What can thermal inertia do for you? (abstract 1144) [CD-ROM], *Lunar Planet. Sci.*, XXXIII, 2002.
- Presley, M. A., and P. R. Christensen, Thermal conductivity measurements of particulate materials: 2, Results, *J. Geophys. Res.*, 102, 6551–6566, 1997.
- Ramsey, M. S., and P. R. Christensen, Mineral abundance determination: Quantitative deconvolution of thermal emission spectra, *J. Geophys. Res.*, 103, 577–596, 1998.
- Ramsey, M. S., P. R. Christensen, N. Lancaster, and D. A. Howard, Identification of sand sources and transport pathways at the Kelso Dunes, California, using thermal infrared remote sensing, *Geol. Soc. Am. Bull.*, 111, 646–662, 1999.
- Sagan, C., D. Pieri, P. Fox, R. E. Arvidson, and E. A. Guinness, Particle motion on Mars inferred from the Viking Lander cameras, *J. Geophys. Res.*, 82, 4430–4438, 1977.
- Scott, D. H., and K. L. Tanaka, Geologic map of the western equatorial region of Mars, *U.S. Geol. Surv. Misc. Invest. Map, I-1802-A*, scale 1:15,000,000, 1986.
- Singer, R. B., and H. Y. McSween Jr., The igneous crust of Mars: Compositional evidence from remote sensing and the SNC meteorites, in *Resources of Near-Earth Space*, edited by J. S. Lewis et al., pp. 709–736, Univ. of Ariz. Press, Tucson, 1993.
- Smith, M. D., J. L. Bandfield, and P. R. Christensen, Separation of atmospheric and surface spectral features in Mars Global Surveyor Thermal Emission Spectrometer (TES) spectra, *J. Geophys. Res.*, 105, 9589–9607, 2000.
- Soderblom, L. A., The composition and mineralogy of the Martian surface from spectroscopic observations: 0.3  $\mu\text{m}$  to 50  $\mu\text{m}$ , in *Mars*, edited by H. H. Kieffer et al., pp. 557–593, Univ. of Ariz. Press, Tucson, 1992.
- Strom, R. G., S. K. Croft, and N. G. Barlow, The Martian impact cratering record, in *Mars*, edited by H. H. Kieffer et al., pp. 383–423, Univ. of Ariz. Press, Tucson, 1992.
- Tanaka, K. L., D. H. Scott, and R. Greeley, Global stratigraphy, in *Mars*, edited by H. H. Kieffer et al., pp. 345–382, Univ. of Ariz. Press, Tucson, 1992.
- Thomas, P., Present wind activity on Mars: Relation to large latitudinally zoned sediment deposits, *J. Geophys. Res.*, 87, 9999–10,008, 1985.
- Thomson, J. L., and J. W. Salisbury, The mid-infrared reflectance of mineral mixtures (7–14  $\mu\text{m}$ ), *Remote Sens. Environ.*, 45, 1–13, 1993.
- White, B. R., Soil transport by winds on Mars, *J. Geophys. Res.*, 84, 4643–4651, 1979.
- Wyatt, M. B., and H. Y. McSween Jr., Spectral evidence for weathered basalt as an alternative to andesite in the northern lowlands of Mars, *Nature*, 417, 263–266, 2002.
- Wyatt, M. B., J. L. Bandfield, H. Y. McSween Jr., and P. R. Christensen, Compositions of low albedo intracrater materials and wind streaks on Mars: Examination of MGS TES data in western Arabia Terra (abstract 1872) [CD-ROM], *Lunar Planet. Space Sci.*, XXXII, 2001.
- Zuber, M. T., et al., Internal structure and early thermal evolution of Mars from Mars Global Surveyor topography and gravity, *Science*, 287, 1788–1793, 2000.

P. R. Christensen and D. Rogers, Department of Geological Sciences, Arizona State University, Campus Box 876305, Tempe, AZ 85287-6305, USA. (phil.christensen@asu.edu; deanne.rogers@asu.edu)